An improved firn densification model by integrating the Bucket scheme and Darcy's law over the Greenland Ice Sheet

Xueyu Zhang[1, 2], Lin Liu[1, 2*], Brice Noël[3], and Zhicai Luo[1, 2]

[1]MOE Key Laboratory of Fundamental Physical Quantities Measurement and Hubei Key Laboratory of Gravitation and Quantum Physics, PGMF and School of Physics, Huazhong University of Science and Technology, Wuhan 430074, P. R. China
[2]Institute of Geophysics and PGMF, Huazhong University of Science and Technology, Wuhan 430074, P. R. China
[3]Laboratoire de Climatologie et Topoclimatologie, University of Liège, Liège, Belgium

Correspondence to: Lin Liu (liulin616@hust.edu.cn)

Abstract. Modelling firn densification is conducive to enhancing the accuracy of monitoring glacier mass changes from satellite altimetry and extracting climate records from ice cores. As snowmelt is increasing in a warming climate on the Greenland Ice Sheet (GrIS), quantifying the role of liquid water within the firn layer becomes critical for simulating firn properties. Nevertheless, previously published firn densification models do not accurarely capture the extensive density fluctuations caused by liquid water refreezing in observations. In this study, an improved firn densification model is developed by integrating the Bucket scheme and Darcy's law to assess the capillary retention, refreezing, and runoff of liquid water within the firn layer. Moreover, the improved model is employed for two study sites, KAN_U and Dye-2, over the GrIS to evaluate its performance. At the KAN_U site, characterized by high snowfall and snowmelt rates, the model captures high-density peaks (~917 $kg \cdot m^{-3}$) caused by the refreezing of liquid water, which corresponds to the formation of ice lenses or ice layers. At Dye-2 with comparatively limited liquid water, the model also captures the features of high-density layers resulting from refreezing. In general, the modelled firn depth-density profiles at the two study sites agree well with the in situ measurements obtained from 12 firn cores drilled between 2012 and 2019. For the regions with limited liquid water, low-density peaks are probably overestimated due to excess refreezing or limited knowledge of ice lenses or ice layers. Future work is expected to enhance the understanding and further improve numerical simulation of the mechanisms involved in firn densification, and subsequently integrate data-driven and physical mechanisms into firn densification modelling.

1 Introduction

Firn densification refers to an intermediate stage in the transition from fresh snow to glacier ice. Given the absence of suitable methodologies or techniques for directly measuring firn properties throughout the Greenland Ice Sheet (GrIS), the characteristics of firn are typically obtained through the modelling of firn densification (Ligtenberg et al., 2011; Morris and Wingham, 2015; Smith et al., 2020). Firn densification models have two primary applications in glaciology: (i) enhancing the

accuracy of estimating the glacier mass balance from satellite altimetry and (ii) assisting in extracting climate records from ice cores (Stevens et al., 2023). Satellite altimetry is an accurate and robust approach to monitor glacier mass balance (Shepherd et al., 2012, 2020; Helm et al., 2014), in which elevation changes are determined by repeated scanning of the glacier surface with satellite altimeters (Huss et al., 2013). A crucial step to convert the elevation-change (volume) measurements to mass

35   change is to determine the firn density associated with the elevation change, which is often estimated by a firn densification model (Brils et al., 2022). Accurately calculating the age difference between the gas trapped within bubbles and the surrounding ice enables to reconstruct the historical climate from ice cores (Lundin et al., 2017). The specific method involves using a firn densification model to predict the age of the firn at the pore close-off depth and a firn-air model to estimate the average age of gases enclosed within closed bubbles (Buizert et al., 2016).

40

In the past few decades, numerous firn densification models have been developed, which can be used to estimate the depth-density or depth-age profiles. According to complexity and physical mechanisms implemented, these models are classified into empirical, semi-empirical, and physical models. Empirical or semi-empirical models are typically represented as mathematical functions of temperature and accumulation rate (e.g., Herron and Langway, 1980; Zwally et al., 2002; Li et al.,

45   2004, 2011; Ligtenberg et al., 2011; Simonsen et al., 2013; Kuipers Munneke et al., 2015). Utilizing the observed firn depth-density profiles for calibration enhances the applicability of empirical or semi-empirical models in the calibration region. However, the observations used for model calibration may not be representative of future firn densities in a warming climate (Ligtenberg et al., 2018), potentially rendering these models unable to provide reliable future predictions. Physical models utilize the inherent material characteristics of snow and firn to replicate the densification process (Alley, 1987; Arnaud et al.,

50   2000). The development of physical models progresses slowly due to a limited knowledge of the physical mechanisms governing firn densification. Both empirical, semi-empirical, and physical firn models have been used in Greenland and Antarctica. Nevertheless, these models usually ignore or provide simplified representations of processes associated with liquid water, thereby having certain limitations when applied to sites with substantial liquid water (Thompson-Munson et al., 2023).

55   Glacier areas experiencing snowmelt and rainfall have expanded with the warming climate over the past decade. In particular, a succession of extreme surface melt events has been documented over the GrIS, with most of the ablation occurring in the northwest and south (Lu et al., 2015). In July 2012, an unprecedented melt event occurred, with surface melt encompassing nearly the entire GrIS (Nghiem et al., 2012). In the summer of 2019, the GrIS experienced the most significant annual ice loss since 1948 (Tedesco et al., 2020). The production of liquid water on the GrIS, thus, is becoming increasingly significant as

60   snowmelt rates increase further in response to global warming. When liquid water appears on the surface of the firn column, it tends to infiltrate further into the column. After that, it may either remain in a liquid form in the firn's pore space (Forster et al., 2014), or refreeze within the firn layer, or depart from the firn column by runoff when encountering an impermeable layer (Machguth et al., 2016). Specifically, refreezing of liquid water within the firn produces ice lenses (thinner than 0.1 m) or ice layers (between 0.1 and 1 m thick), both of which can accumulate into low-permeability ice slabs (thicker than 1 m) (MacFerrin

65   et al., 2022). Upon encountering a thick ice slab, liquid water reduces or even stops percolation, thus leaving the firn column
through runoff. Liquid water refreezing is a crucial process in firn densification, primarily influencing firn properties through
two levels. Firstly, the release of latent heat during refreezing has the potential to induce a notable increase in firn temperature,
further accelerating the rate of firn densification. Besides, stress exerted by ice lenses or ice layers further compresses and
densifies firn, thus leading to a higher density within the firn layer.

70

The Bucket percolation scheme is commonly used to simulate the vertical transport of liquid water in the firn column, in which
the firn column is divided into numerous layers and water tips from one layer to the next within one time step (Jin et al., 1999).
The implementation of the bucket scheme in firn densification models does not capture the complex liquid water processes
related to ice slab formation (Kuipers Munneke et al., 2015; Verjans et al., 2019; Thompson-Munson et al., 2023). Hirashima
75   et al. (2010) developed a water balance scheme where water flows downward by Darcy's law, which relates the water flux to
the hydraulic conductivity and capillary suction, potentially considering gravity and capillary forces. The Darcy-flow scheme
was found to delay the percolation enough to allow liquid water to refreeze in place rather than percolate and spread through
several layers (Stevens et al., 2018). Langen et al. (2017) applied Darcy's law to their firn densification model. Commencing
from a depth of 4 m, modelled firn density remains stable at roughly 800 kg m^{-3} at KAN_U and 700 kg m^{-3} at Dye-2, two
80   sites of the GrIS, which does not capture the observed extensive density fluctuations. The two aforementioned liquid water
flow schemes assume uniform infiltration of liquid water, known as matrix flow. However, heterogeneous flow, referred to as
preferential flow, has been demonstrated to play a crucial role in liquid water transport (Pfeffer et al., 1996; Humphrey et al.,
2012). To reproduce the occurrence of dense ice layers in a seasonal alpine snowpack, Wever et al. (2016) proposed a dual-
domain approach in which the pore space is divided into two parts: one represents matrix flow and the other represents
85   preferential flow. Richards' equation, which is often applied to soils to describe variably saturated matrix flow (Richards, 1931),
is then solved for both domains and only water in matrix flow is subjected to phase changes. It is found that around 20% of
observed ice layers in the field were correctly simulated by this dual-domain approach (Wever et al., 2016). However, Verjans
et al. (2019) showed that implementing such a dual-domain approach in firn densification models did not improve upon the
simple bucket scheme when compared to observed data.

90

In this study, a firn densification model considering liquid water percolation and phase-change mechanisms has been developed
by integrating the Bucket scheme and Darcy's law, with its upper boundary driven by the polar version of the Regional
Atmospheric Climate Model (RACMO2.3p2; Noël et al., 2019). We assumed that liquid water behaved as a Newtonian fluid,
and both gravity and capillary forces influenced its flow within the firn column. Afterward, the Bucket scheme and Darcy's
95   law were coupled to simulate the percolation and refreezing of liquid water during firn densification. Moreover, recently
published parametrizations for surface density and thermal conductivity were utilized to establish parametrizations for fresh-
snow density and firn temperature. A conventional grain growth rate equation is employed to calculate the radius of firn grains.
Since liquid water primarily affects firn density by temperature, a firn model centered on temperature sensitivity was applied

to simulate dry-firn compaction. The firn densification model was then applied to simulate the firn depth-density profile in two
100   climatologically distinct sites of the GrIS: one characterized by high snowfall and snowmelt rates (KAN_U) and the other by
comparatively low snowfall and snowmelt rates (Dye-2).

2 Data

2.1 Climatic forcing

The forcing data of the model used in this study were snow accumulation, liquid water, and skin temperature. Snow
105   accumulation was obtained by subtracting sublimation and snowmelt from snowfall. Liquid water was the combination of
snowmelt and rainfall, where rainfall was the difference between total precipitation and snowfall. Restricted by the availability
of observational data in terms of time and space, these climatic data were typically collected from regional climate models
(RCMs). The RCMs commonly employed for the investigation of meteorological and climatic characteristics of the GrIS
involve RACMO2.3p2 (the Regional Atmospheric Climate Model version 2.3p2), MAR (the Modèle Atmosphérique Régional),
110   PROMICE (Programme for Monitoring of the Greenland Ice Sheet), and HIRHAM (the High-Resolution Limited-Area Model).
By comparing these RCMs to in situ meteorological data and point SEB/SMB measurements, the accuracy of RACMO2.3p2
is higher than the other models over the GrIS (Noël et al., 2018; Fettweis et al., 2020; Van Dalum et al., 2021). Therefore, in
order to precisely simulate the firn depth-density profiles, the atmospheric forcing of the model was collected from
RACMO2.3p2.

115

RACMO2.3p2 is forced at the lateral boundaries by a combination of European Centre for Medium-Range Weather Forecasts
(ECMWF) reanalysis datasets from ERA-40 over 1958-1978, ERA-Interim over 1979-1989, and ERA5 over 1990-2020 (Noël
et al., 2019). The data of snowfall, snowmelt, total precipitation, and sublimation were statistically downscaled on a daily basis
from RACMO2.3p2 at 5.5 km resolution onto a 1 km grid for the period 1958-2020. In addition, skin temperature was available
120   on daily basis for the same time period but on the native RACMO2.3p2 grid at 5.5 km. The forcing from RACMO2.3p2 has
been demonstrated to yield significant improvements in modelled firn densification (Ligtenberg et al., 2018).

2.2 Study sites

In this research, case studies were conducted at KAN_U (67.00° N, 47.02° W) and Dye-2 (66.48° N, 46.28° W), two study
sites in the percolation zone of the GrIS (Fig. 1). The selection of these two sites was motivated by their variety in climatic
125   characteristics: one with relatively high snowmelt rates and the other with relatively low snowmelt rates. These climatic
characteristics render KAN_U and Dye-2 suitable for assessing the applicability of the firn densification model in regions
representing different snowmelt rates. Table 1 summarizes the geographical and climatological information of the two study
sites. Situated in the southwest and at a lower elevation, KAN_U experienced a slightly higher annual mean surface
temperature (-16.79℃) than Dye-2 (-18.34℃) between 1958 and 2020, resulting in higher snowmelt rates. Specifically,

130   KAN_U exhibited an annual mean snowmelt of 282.83 mm w.e. (water equivalent) during this period, and meanwhile, Dye-2 displayed corresponding values of 145.97 mm w.e. With the increase in surface temperature of the GrIS over the past two decades, both snowfall and snowmelt have undergone changes. As exhibited in Fig. 2, a slight reduction in snowfall and an increase in snowmelt have been observed in KAN_U since 2008. In particular, the annual cumulative snowmelt exceeded the annual cumulative snowfall in the warm years of 2010, 2012, 2016, and 2019. At Dye-2, the typical annual cumulative

135   snowmelt ranges between 39 and 310 mm w.e. (Fig. 3). Except for the extreme melt year of 2012 (Nghiem et al., 2012), which exhibited a striking peak of 676.14 mm w.e.

Characterized by distinct climatic conditions, the mechanism of firn densification thus differs in the two sites. Abundant snowfall and moderate snowmelt at Dye-2 render it a representative percolation zone, where meltwater generated at the surface

140   percolates into the firn and releases latent heat when refreezing into ice lenses or ice layers. Snowmelt favors the formation of ice slabs in KAN_U, impeding the further infiltration of liquid water at depth and facilitating liquid water runoff (MacFerrin et al., 2019). Previous work developed models based on the water flow programs driving densification and evaluated the model performance at Dye-2 or KAN_U (Langen et al., 2017; Verjans et al., 2019; Vandecrux et al., 2020b; Brils et al., 2022). In comparison with in situ measurements, these firn models usually underestimate high-density peaks caused by ice lenses or ice

145   layers, which will be discussed in detail in Sect. 4.
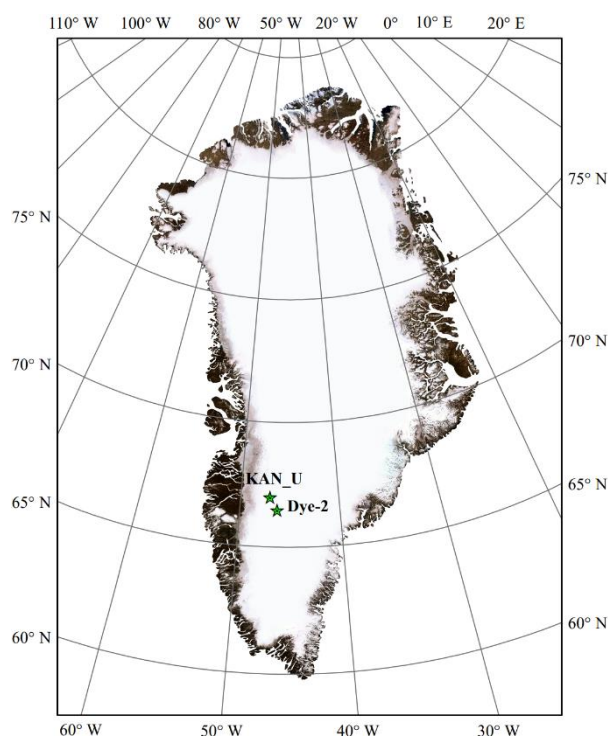
Figure 1. Map of the two study sites on the Greenland Ice Sheet.

Table 1. Information about the two study sites, including annual mean surface temperature, snowfall and snowmelt (1958-2020).

Site	Latitude (°)	Longitude (°)	Elevation (m)	Annual mean surface temperature (℃)	Annual mean snowfall (mm w.e.)	Annual mean snowmelt (mm w.e.)
KAN_U	67.00	-47.02	1840	-16.79	517.26	282.83
Dye-2	66.48	-46.28	2119	-18.34	469.05	145.79
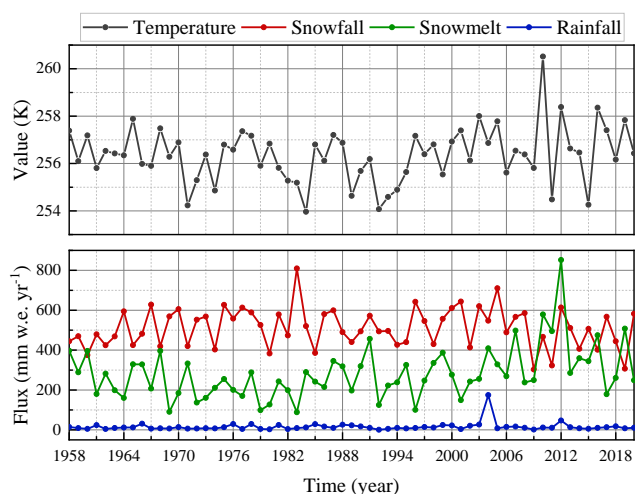
Figure 2. Time series of the annual mean surface temperature, annual cumulative snowfall, snowmelt and rainfall from RACMO2.3p2 at KAN_U (1958-2020).
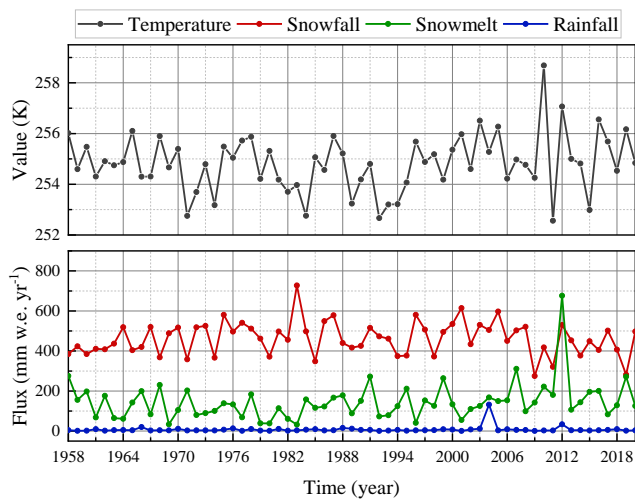
Figure 3. Time series of the annual mean surface temperature, annual cumulative snowfall, snowmelt and rainfall from RACMO2.3p2 at Dye-2 (1958-2020).

2.3 Observation data

160 The most common method for evaluating the performance of a firn densification model is to compare the modelled firn density
with the observed density profiles obtained from firn cores (Herron and Langway, 1980; Helsen et al., 2008; Ligtenberg et al.,
2011) or from laboratory experiments (Zwally et al., 2002). In this study, the observed depth-density profiles used for
evaluation were sourced from the Surface Mass Balance and Snow on Sea Ice Working Group (SUMup) dataset (Thompson-
Munson et al., 2022), which included in situ observations of firn density on both ice sheets. For each study site, the vertical

165 density profiles from firn cores closest to that location were employed to evaluate the performance of the firn densification
model. A total of 12 firn cores, ranging in depth from 7.8 m to 26.45 m, were selected for this study. These cores were primarily
drilled in late April or May between 2012 and 2019, coinciding with substantial snowmelt, which provided an optimal condition
for observing firn density in the presence of liquid water. Detailed characteristics and specific drilling dates for these 12 firn
cores are listed in Table 2. In the date column, '2012-05-00' denotes that the firn core was drilled in May 2012, with the specific

170 day being unknown.

Table 2. Characteristics of firn cores used for model evaluation.

Site	Date	Latitude (°)	Longitude (°)	Elevation (m)	Initial depth of borehole top (m)	Initial depth of borehole bottom (m)
KAN_U	2012-05-00	66.99825	-47.020832	1840	0.17	10.21
	2013-04-28	67.00025	-47.0221329	1840	0.79	15.88
	2015-05-04	67.00042	-47.024715	1840	0.65	14.35
	2016-04-26	67.00038	-47.026150	1838	0	7.8
	2016-04-28	67.00038	-47.026150	1838	0	16.41
	2017-04-28	67.00025	-47.022633	1840	0.78	23.19
Dye-2	2013-05-04	66.47260	-46.282982	2119	0.09	16.45
	2015-05-20	66.47771	-46.286060	2126	0.81	19.21
	2016-05-06	66.47260	-46.282982	2126	0	17.21
	2017-05-13	66.47804	-46.287125	2112	0	26.45
	2018-05-09	66.47787	-46.286740	2112	0	19.62
	2019-05-19	66.47805	-46.288701	2113	0	20.975

3 Firn densification model

After settling to the surface, fresh snow undergoes compaction under the forcing of gravity and overburden stress. Meanwhile,
175 the liquid water composed from snowmelt and rainfall will percolate downward into the firn column due to the porosity and

permeability of the firn grains. Liquid water will refreeze and form ice lenses or ice layers when reaching a firn layer with sufficient cold content and pore space. To clarify, cold content is the energy required to raise the temperature of the firn to melting temperature (Langen et al., 2017). Due to capillary forces, a portion of liquid water is retained within the firn layer, unable to percolate farther or refreeze. In addition, once liquid water encounters a thick ice slab formed by ice lenses or ice layers, it is challenging to percolate further and thus departs from the firn column through runoff (Fig. 4a).

180

In order to study the distribution and proportions of liquid water among retention, refreezing, and runoff, we establish a 1D vertical Lagrangian model with the vertically downward direction as the positive direction (Fig. 4b). The vertical coordinate, z, increases downwards. Subsequently, the firn column is divided into a finite number of firn layers, each with a thickness denoted as dz. The solid input of the firn column is derived from the difference between snowfall and sublimation, and the liquid input originates from snowmelt and rainfall. New added surface snow is instantly treated as the upper layer of the vertical firn column while removing one firn layer from the bottom of the firn column. Every individual firn layer is partitioned into distinct contributions from firn, ice, and liquid water, with each component expressed in terms of m w.e. units. Due to the varying proportions of these three components, firn properties change from layer to layer. However, within each layer, firn properties are assumed to remain constant. Thus, we keep track of the density and temperature of each firn layer during their downward motion to simulate the depth-density and depth-temperature profiles.

185

190
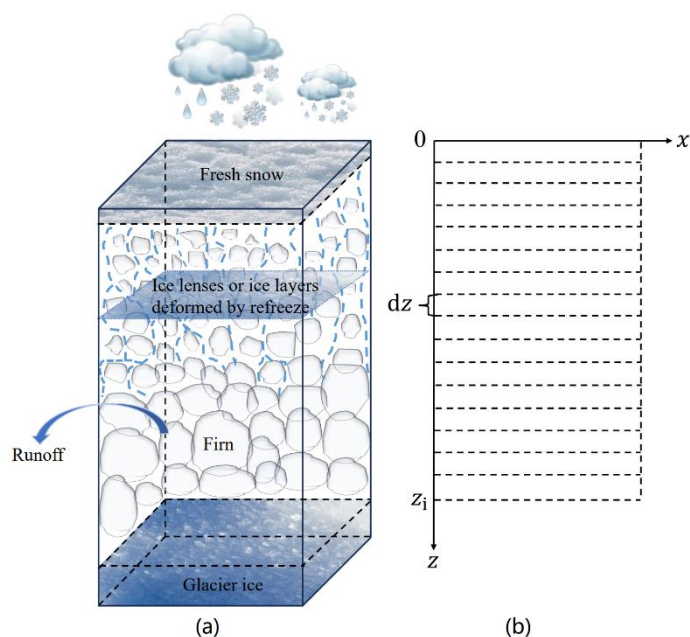
Figure 4. Schematic representation of firn densification processes (a) and simple layering scheme used in this study (b).

195

In this research, fresh-snow density, a critical boundary condition for the model, is prescribed with an empirical parameterization that depends on annual mean surface temperature (Sect. 3.1). Firn temperature is solved by a one-dimensional heat-transfer equation (Sect. 3.2). A conventional grain growth rate equation was employed to simulate the increase in grain radius, based on the assumption that firn was composed of spherical grains, and the growth of these grains was characterized
200 by radial expansion starting from the center (Sect. 3.3). The model of Li et al. (2011) is utilized to simulate dry-firn compaction given its temperature sensitivity (Sect. 3.4). Liquid water scheme, in this work, is a combination of the Bucket scheme and Darcy's law to consider liquid water percolation and phase-change mechanisms (Sect. 3.5). By integrating the dry-firn compaction model, which determines firn density independently of liquid water, with the liquid water scheme that calculates the density increment caused by liquid water refreezing, we simulate the depth-density profiles of the firn (Sect. 3.6).

205

3.1 Fresh-snow density

An essential boundary condition for the model is the density of the first firn layer on the firn column, ρ_s. Fresh-snow density is typically stated as a constant value, like $350 \ \mathrm{kg \ m^{-3}}$ (Stevens et al., 2020), or as a function of meteorological variables such as temperature and wind speed (Keenan et al., 2021). Considering the dynamic nature of atmospheric conditions, which
210 leads to a certain variability in surface density, a parameterized equation may provide a more realistic approximation of actual fresh-snow density than a constant value. Differing from earlier investigations, which typically use the first 1.0 m of snow (Kuipers Munneke et al., 2015) and thus systematically overestimate the actual snow density at the surface, Fausto et al. (2018) focused only on the upper 0.1 m of snow at 200 locations of the GrIS to develop a parameterization for fresh-snow density and found:

215   $$\rho_s = 362.1 + 2.78 \cdot T_a, \tag{1}$$

Here, T_a is the annual mean near-surface (usually 2 m) air temperature (℃). Although the actual density of fresh snow could vary with each accumulation event, the parameterization is derived by fitting the measured snow densities to mean annual temperatures. Therefore, in this model, T_a is calculated as the average near-surface air temperature of the year preceding the accumulation event to avoid introducing an additional uncertainty.

220   ### 3.2 Grain growth and microstructure evolution

The continuous accumulation of fresh snow subjects the underlying firn layer to augmented stress. Stress disparities develop at grain boundaries due to variations in grain boundary curvature and stored strain energy among crystal grains. High-stress regions on concave surfaces interacting with low-stress regions on other surfaces give rise to an unstable state, prompting grain boundary sliding and causing a rearrangement of grain structures. As a result, the system composed of grains undergoes motion
225 aimed at minimizing surface area, leading to a gradual engulfing of smaller crystals by bigger ones, a phenomenon usually known as grain growth.

The shape of firn grains is typically depicted as sphericity or dendricity. Considering the challenges associated with simulating dendritic grain growth and the lack of relevant laboratory observations and model simulations, we simulate firn grains as

230   spherical grains. Grain growth is then simulated as a process of radius expansion around the grain's center. Hence, the radius of a particle $r(t)$ is determined from an initial radius r_0 and the growth rate R_g as a function of time:

$$r^2(t) = R_g t + r_0^2, \tag{2}$$

The Arrhenius equation is used to calculate the growth rate R_g, which is a function of rate constant R_0, grain-growth activation energy E_g, gas constant R, and firn temperature T:

235   $$R_g = R_0 \exp(-\frac{E_g}{RT}), \tag{3}$$

The above parameterization assumes linear grain growth under isothermal conditions. In the literature, values of E_g vary between $47\,\text{kJ}\,\text{mol}^{-1}$ (Gow, 1969) and $42.4\,\text{kJ}\,\text{mol}^{-1}$ (Cuffey et al., 2010). Following Arthern et al. (2010), we set R_0 to be $0.13\,\text{mm}^2\,\text{s}^{-1}$ and E_g to be $42.4\,\text{kJ}\,\text{mol}^{-1}$, where R_0 is calculated by assuming spherical grains with average cross-sectional area $2\pi r^2/3$. The initial grain radius, r_0, usually is prescribed as a constant value, such as 0.1 mm (Katsushima et

240   al., 2009). In this study, we use the empirical formula obtained from Linow et al. (2012) to calculate the initial grain radius:

$$r_0\left(\bar{T}, \bar{b}\right) = b_0 + b_1\bar{T} + b_2\bar{b}, \tag{4}$$

with $b_0 = 0.781$, $b_1 = 0.0085$, $b_2 = -0.279$. Therefore, r_0 is a function of mean annual temperature $\bar{T}$ (℃) and mean annual accumulation rate $\bar{b}$ (m w. e. a^{-1}), and it remains constant throughout each time step.

3.3 Firn temperature evolution

245   Surface snow metamorphism and firn densification depend on thermal conditions (Calonne et al., 2019). Therefore, understanding how temperature fluctuations propagate through the firn column is essential. The vertical temperature distribution and its evolution are simulated by solving a one-dimensional and time-dependent heat-transfer equation:

$$c_f \frac{\partial T}{\partial t} = \frac{dK}{dz} \cdot \nabla T + K \cdot \nabla^2 T + Q_L, \tag{5}$$

In this equation, K is the thermal conductivity of the firn, which is related to firn density and firn temperature, thus $\frac{dK}{dz} =$

250   $\frac{\partial K}{\partial \rho}\frac{\partial \rho}{\partial z} + \frac{\partial K}{\partial T}\frac{\partial T}{\partial z}$; c_f is the specific heat capacity of the firn; Q_L is a heat source representing the release of latent heat during the refreezing of liquid water in the firn layer. The value of Q_L corresponds to the latent heat released in the preceding time step, which is thus set to 0 for the initial time step.

Firn thermal conductivity, a crucial factor in simulating heat diffusion, is extensively investigated based on field and laboratory

255   experiments (Van Dusen and Washburn, 1929; Schwerdtfeger, 1963; Yen, 1981; Sturm et al., 1997; Calonne et al., 2011). Nevertheless, no universally accepted parameterization exists for firn thermal conductivity, and most of the existing predictive formulas are developed for a given temperature or density range, rendering them inapplicable at temperatures or densities

outside of the provided range. Calonne et al. (2019) developed a parameterization of firn thermal conductivity from 3-D images of snow, firn, or porous ice microstructures, covering a density range from 100 to 888 kg m^{-3}, at different temperatures. This

260   parameterization has been confirmed to be valid for a wide range of temperatures and densities typically observed in the firn layers of ice sheets, making it appropriate for simulations of the GrIS, and it is represented as:

$$K(\rho, T) = (1 - \theta) \frac{k_i(T)k_a(T)}{k_i^{ref}k_a^{ref}} k_{snow}^{ref}(\rho) + \theta \frac{k_i(T)}{k_i^{ref}} k_{firn}^{ref}(\rho), \tag{6}$$

This parameterization equation consists of two parts: one for snow and low-density firn and one for ice and high-density firn. The transition between the two components remains smooth through the weight factor $\theta(\rho)$. The definition of θ and the

265   thermal conductivities used in Eq. (6) are

$$\theta = 1/(1 + \exp(-0.04(\rho - 450)), \tag{7}$$

$$k_{firn}^{ref}(\rho) = 2.107 + 0.003618(\rho - \rho_i), \tag{8}$$

$$k_{snow}^{ref}(\rho) = 0.024 - 1.23 \times 10^{-4}\rho + 2.5 \times 10^{-6}\rho^2, \tag{9}$$

$$k_i(T) = 9.828\exp(-5.7 \times 10^{-3}T), \tag{10}$$

270   $$k_a(T) = (2.334 \times 10^{-3}T^{3/2})/(164.54 + T), \tag{11}$$

where, $\rho_i = 917$ kg m^{-3} is taken to be the density of ice, $k_i(T)$ and $k_a(T)$ represent the thermal conductivity of ice and air at temperature T, respectively. Here, $k_a(T)$ is taken from Reid et al. (1959). Moreover, $k_i^{ref} = 2.107$ W $\cdot$ m$^{-1} \cdot$ K^{-1} and $k_a^{ref} = 0.024$ W $\cdot$ m$^{-1} \cdot$ K^{-1} represent the thermal conductivity of ice and air, respectively, at the reference temperature of $-3℃$.

275   **3.4 Dry-firn compaction model**

As mentioned above, with the accumulation of new snow at the surface (the top of the firn column), the firn layers are buried deeper and tracked during their downward motion. At every time step, each layer is compacted under the stress exerted by the gravity of snow/firn above it. In this research, the densification rate is not directly related to the overburden stress, but rather employs the accumulation rate as a proxy. The firn densification model of Li et al. (2011) (the following is called the LZ-2011

280   model) provides the dry-firn compaction scheme for our simulations, which accounts for the temperature dependence of both grain growth and ice creep on firn compaction by introducing a temperature-dependent activation energy. Here, we choose the LZ-2011 model as the dry-firn compaction model for two reasons.

Firstly, it is assumed that the densification rate of wet firn is equal to that of dry firn. We acknowledge that the presence of

285   liquid water between firn grains could impact the evolution of firn size and shape, which in turn may also impact the densification rate of the firn. However, due to a lack of physical understanding and available measurements, we have decided not to introduce an additional dependence of the liquid water content on the compaction rate to reduce model complexity and prevent overfitting. Instead, we simulate the impact of liquid water on firn density by considering how it affects the firn layer's mass and temperature as it refreezes into ice (Sect. 3.5).

290

Secondly, the primary manner liquid water promotes densification is via the latent heat released during refreezing. Latent heat will raise the firn's temperature and accelerate the firn densification rate. The LZ-2011 model is a firn compaction model developed for the GrIS, taking temperature sensitivity and vapor diffusion mechanisms into account. Therefore, employing the temperature-sensitive LZ-2011 model as the dry-firn compaction model will assist us in assessing the force of liquid water on

295   firn densification with greater certainty.

The constitutive function of the LZ-2011 model is

$$\frac{\mathrm{d}\rho}{\mathrm{d}t} = \beta 8.36 T_{\mathrm{c}}^{-2.061} \dot{b}(\rho_{\mathrm{i}} - \rho),   \quad (12)$$

where, β is a stage-dependent adjustable parameter determined by fitting modelled depth-density profiles to field

300   measurements. Li et al. (2011) present value of β as a function of annual mean temperature, $T_{\mathrm{c}} = T - 273.15$ (℃), and long-term accumulation rate, $\dot{b}$ (m w. e. a^{-1}). For the GrIS, β is represented as:

$$\beta = \beta_1 = -9.788 + 8.996\dot{b} - 0.6165 T_{\mathrm{c}}   \quad (\rho \le 550 \, \mathrm{kg} \cdot \mathrm{m}^{-3}),   \quad (13)$$

$$\beta = \beta_2 = \beta_1/(-2.0178 + 8.4043\dot{b} - 0.0932 T_{\mathrm{c}})   \quad (\rho > 550 \, \mathrm{kg} \cdot \mathrm{m}^{-3}),   \quad (14)$$

3.5 Liquid water scheme

305   As long as liquid water is available at the surface and the porosity of the firn allows percolation, water will percolate to a deeper layer by gravitation. Percolation proceeds until all the water is depleted or until it reaches an impermeable layer, where all the water in excess is instantly treated as lateral runoff. Our model employs a combination of the Bucket scheme and Darcy's law to treat water percolation, capillary retention, and refreezing. For some firn layers, the pore space can accommodate both air and water. The variable P is used to denote the porosity of a firn layer with a thickness of $\mathrm{d}z$, which

310   is defined as the ratio of the volume of pore space inside the firn layer to the total volume of the firn layer and calculated from the firn density and ice density: $P = 1 - \rho/\rho_{\mathrm{i}}$. Consequently, the pore space within the firn layer, denoted as φ, is determined by multiplying the porosity P by the thickness of the layer $\mathrm{d}z$. The vertical firn water flux depends on the firn's irreducible water content (Coléou and Lesaffre, 1998), the firn's saturated (Calonne et al., 2012) and unsaturated (Hirashima et al., 2010) hydraulic conductivities, and a coefficient that accounts for the effect of ice content on the firn hydraulic conductivity (Colbeck,

315   1975). We, therefore, establish the liquid water scheme in three segments: water saturation, liquid water content, and refreezing.

3.5.1 Water saturation

The maximal pore space that can be occupied by liquid water is known as the saturated water volume. Considering the volume expansion resulting from the refreezing of all liquid water present within the pore spaces into ice, the saturated water content is expressed as: $\theta_{\mathrm{s}} = V_{\mathrm{wm}}/\mathrm{d}z$, where the saturated water volume $V_{\mathrm{wm}} = \varphi * (\rho_{\mathrm{i}}/\rho_{\mathrm{w}})$. Due to the forcing of capillary and

320   adhesive forces, a small fraction of the water will be retained within some of the available pore space of the firn layer and not

subject to vertical transfer, which is often referred to as irreducible water. The maximum water saturation that can be sustained by the capillary tension of firn grains is termed the water-holding capacity, S_{wi}, with values employed in models varying widely (Langen et al., 2017). For example, a common practice is to use constant values (Colbeck et al., 1974; Yamaguchi et al., 2010; Reijmer et al., 2012; Steger et al., 2017). In this study, we follow the formulation from Coléou and Lesaffre (1998), where the water-holding capacity S_{wi} is taken as a function of firn density ρ:

$$S_{wi} = \frac{W_{mi}}{1-W_{mi}} \frac{\rho_i \rho}{\rho_w(\rho_i-\rho)}, \tag{15}$$

$$W_{mi} = 0.057 \frac{\rho_i-\rho}{\rho} + 0.017, \tag{16}$$

Assuming the liquid water volume within one firn layer is V_w, thus the irreducible water content θ_i, is represented as: $\theta_i = V_{wi}/dz$, with $V_{wi} = V_w * S_{wi}$. Finally, the effective water saturation can be expressed as

$$\Theta = \frac{\theta_w - \theta_i}{\theta_s - \theta_i}, \tag{17}$$

where $\theta_i < \theta_w < \theta_s$, the liquid water content θ_w is given as the ratio of V_w to dz.

3.5.2 liquid water content

Water in excess of the irreducible water content is allowed to move downward. Because firn is a porous material, water flow in the firn column can be estimated using Darcy's law. Water flux q is a function of hydraulic conductivity K_w and capillary suction h:

$$q = K_w(\frac{dh}{dz} + 1), \tag{18}$$

Here, dh/dz is the vertical hydraulic gradient in capillary suction, and the second term $(+1)$ represents gravity due to the hydraulic gradient including the combined effects of capillary and gravitational forces for unsaturated firn layers. Porosity and pore structures influence capillary suction and hydraulic conductivity. However, characterizations such as pore shape, pore connectivity, and tortuosity are difficult to measure or simulate directly. In this study, the hydraulic conductivity and the capillary suction are parameterized in terms of firn grain radius r, effective liquid saturation Θ, and firn density ρ. Shimizu (1970) formulated a saturated hydraulic conductivity based on laboratory experiments using kerosene, showing that hydraulic conductivity can be estimated as a function of grain size and snow density:

$$K_s = 0.308 \frac{g}{v_w} r^2 \exp(-0.0078\rho), \tag{19}$$

Here, g is the acceleration due to gravity $(m \cdot s^{-2})$, and $v_w = 1.787 \times 10^{-6}$ m^2 s^{-1} is the kinematic viscosity of water. Van Genuchten (1980) developed an accurate expression for the capillary suction in soil, and Hirashima et al. (2010) further optimized the expression:

$$h = \frac{1}{\alpha}(\Theta^{-\frac{1}{m}} - 1)^{\frac{1}{n}}, \tag{20}$$

In this equation, $\alpha = 14.6r + 1.9$, $n = 15.68 \exp(-0.92r) + 1$, $m = 1 - \frac{1}{n}$. Van Genuchten (1980) combined the theory of Mualem (1976) to estimate the unsaturated hydraulic conductivity, K_r, as follows:

$$K_r = \Theta^{\frac{1}{2}}[1 - (1 - \Theta^{\frac{1}{m}})^m]^2, \tag{21}$$

The hydraulic conductivity of firn can be expressed as the multiplication of the saturated hydraulic conductivity K_s, and the unsaturated hydraulic conductivity K_r, resulting in $K_w = K_s * K_r$. Furthermore, the ice lenses or ice layers formed by refreezing have the potential to impede the infiltration of liquid water. The effect is parameterized by introducing an additional

355   permeability factor K_f, leading to the equation $K_w = K_s * K_r * K_f$. It is assumed that ice layers with a thickness above 0.5 meters act as impermeable barriers, where the factor K_f is equal to zero, otherwise $K_f = 1$.

Based on the above information, we can calculate the water transport amount within a Darcy time step, usually denoted as $q d\tau$. However, it is suggested that the simulations will become unstable if the water transport amount in a Darcy time step

360   approaches the water content (Hirashima et al., 2010). The Darcy time steps must thus be appropriately selected. Hirashima et al. (2010) pointed out that the limit of the water transport amount in a Darcy time step, q_{lim}, is approximated by the amount needed to reach equilibrium conditions between two adjacent vertical layers. Initially, we assume a value of 60 seconds for $d\tau$ and subsequently iteratively adjust this value to approximate the time required for achieving equilibrium conditions. Finally, the water transport amount in a Darcy time step is given as $q_{lim}[1 - \exp(-\frac{q}{q_{lim}} d\tau)]$ (Hirashima et al., 2010). The liquid

365   water content LW_{in} entering a specific firn layer for a time step is the difference between the total liquid water content for that time step (i.e., the liquid water content entering the first firn layer of the firn column) and the liquid water content (including irreducible water content) in all the layers above that particular firn layer. Therefore, the liquid water content V_w for each firn layer is determined as the minimum value between $q_{lim}[1 - \exp(-\frac{q}{q_{lim}} d\tau)]$ and LW_{in}, summed with the liquid water content V_w' in that same layer from the previous time step. For the first snow layer, V_w' is considered to be zero.

370   Specifically, V_w can be expressed as

$$V_w = \min\left[q_{lim}[1 - \exp(-\frac{q}{q_{lim}} d\tau)], \ LW_{in}\right] + V_w', \tag{22}$$

3.5.3 Refreezing

The refreezing amount of liquid water in a firn layer depends on three physical characteristics: (i) the availability of pore space to host the liquid water, (ii) the availability of cold content to refreeze the liquid water, and (iii) the possibility for liquid water

375   to percolate into the firn layer when conditions (i) and (ii) are met (Vandecrux et al., 2020a). Consequently, we calculate the amount of refreezing for a given firn layer according to its maximum refreezing potential, $refreeze_{cap}$, and the maximum liquid water amount available for refreezing, $V_w - V_{wi}$, within the firn layer:

$$refreeze = \min(refreeze_{cap}, \ V_w - V_{wi}), \tag{23}$$

Given the specific heat capacity of firn, c_f, and the latent heat of fusion, $\mathcal{L}$, the maximum refreezing potential can be defined

380   as

$$\text{refreeze}_{\text{cap}} = \frac{Q_{\text{cold}}}{\mathcal{L}*\rho_{\text{w}}} = \frac{c_{\text{f}}*m_{\text{f}}*(T_{\text{m}}-T)}{\mathcal{L}*\rho_{\text{w}}}, \tag{24}$$

where Q_{cold} is the cold content of the firn layer, m_{f} is the mass of the firn layer, T_{m} is the melting temperature (273.15 K). Subsequently, the latent heat of phase change caused by refreezing can be calculated as: $Q_{\text{L}} = \text{refreeze} * \rho_{\text{w}} * \mathcal{L}$.

3.6 Model runs in firn densification

385 In this study, part of the code describing the processes and/or physical mechanisms mentioned above was derived from the Community Firn Model (CFM; Stevens et al., 2020), which is an open-source, modular firn model framework. Subsequently, we complemented the code with additional components necessary to implement our firn densification model. To obtain the initial firn temperature and density profiles, we carry out a 22-year spin-up using forcing data from 1958 to 1979, which is considered representative of the climate of the preceding few hundred years. Once the depth to the bottom of the firn column

390 (delineated at a density of 917 kg m^{-3}) is attained, the firn column is deemed fully replenished, and the spin-up is completed. Due to variable snow accumulation rates, the time of spin-up can vary significantly, resulting in a self-adaptive time frame where the 22-year climate interval is repeated to provide a time series long enough for a full firn column refreshment. If the spin-up time required is not divisible by 22, we round up to the next integer to exceed the required time. For example, if a location needs an 80-year spin-up, the 22-year climate interval is repeated four times.

395

In many studies, the time step is often set to a constant value, leading to a varied snow accumulation within each time step with different climatic conditions. In fact, a smaller amount of snowfall within a time step is more susceptible to being influenced by wind and is blown from the surface of the firn column, failing to engage in firn densification fully. Using low snow accumulation to run the model may lead to higher stress, consequently overestimating the firn temperature and firn

400 density. Taking this factor into consideration, we define the time step as the time required to accumulate an equal amount of snowfall. Through continuous experimentation, the appropriate snowfall amount is found to be 0.015 m w.e in KAN_U and 0.014 m w.e in Dye-2.

The spin-up procedure is primarily implemented through the following two stages. Initially, the steady-state firn compaction

405 model established by Herron and Langway (1980) is employed to determine the origin firn density ρ_{origin} (kg m^{-3}) for each firn layer at the first time step based on the mean daily temperature T_{mean} (K) and the mean annual snowfall A_{mean} (m w.e a^{-1}). From the second time step onwards, ρ_{origin} is set to the firn density from the preceding time step. Subsequently, the LZ-2011 model is run at each time step from 1958 to 1979 to derive the corresponding densification rate $\mathrm{d}\rho/\mathrm{d}t$. The firn density ρ_{dry} (kg m^{-3}) for each firn layer, when not considering the presence of liquid water, is therefore obtained:

410 $$\rho_{\text{dry}} = \rho_{\text{origin}} + \frac{\mathrm{d}\rho}{\mathrm{d}t} * \mathrm{d}t, \tag{25}$$

Before the spin-up, the firn column is initialized at a constant temperature equal to the annual mean surface temperature. Afterwards, the heat equation is solved iteratively until the solution converges at each time step to emulate the vertical firn

temperature profile. Due to the Lagrangian character of the model, any heat generated by horizontal/vertical deformation of the firn could be neglected (Helsen et al., 2008). Therefore, the initial firn temperature and firn density for the model's main-
415   run is obtained from the outcomes of the last time step of the spin-up procedure.

Subsequently, the firn densification model is run at each time step to obtain the density increment and corresponding firn density and firn temperature for that time step from 1958 to 2020. The density increment $\Delta\rho$ (kg m^{-3}), caused by refreezing within each firn layer is given by:

420    $$\Delta\rho = (\text{refreeze} * \rho_{\mathrm{w}})/dz, \tag{26}$$

Combining Equation (25) and Equation (26), the firn density in each firn layer with the presence of liquid water may be written as

$$\rho = \rho_{\mathrm{dry}} + \Delta\rho, \tag{27}$$

4 Results

425   ### 4.1 Firn density

4.1.1 KAN_U

Located in the southwestern region of the GrIS and characterized by a low elevation, KAN_U experiences warm climatic conditions, and snowmelt events occur every year (282.83 mm w.e. yr^{-1}). These annual snowmelt events significantly impact the physical properties of the firn in the vicinity of the site, causing KAN_U to be an ice slab zone. Based on the initial firn
430   depth-density profile obtained from the spin-up procedure, we run the established firn densification model to calculate the firn density for each firn layer in each time step between 1958 and 2020. The time series of these modelled firn depth-density profiles at KAN_U is displayed in Fig. 5. The absence of layered densities in the bottom-left regions of Fig. 5 is explained by the fact that the spin-up procedure does not involve the liquid water scheme. Ice lenses or ice layers start to form after the main-run of the model implements the liquid water scheme, and they gradually move downward over time. During the period
435   from 1958 to 2020, a 24.7 m thickening was modelled. The rate of thickness augmentation has exhibited a substantial deceleration after the year 2010, associated with a warming climate and increased surface snowmelt. In particular, a striking thinning (~ 0.94 m) was observed between 2010 and 2012, which was highlighted by the red box in Fig. 5. Moreover, as a result of increased snowmelt, high-density firn layers were more densely distributed within the 0-10 m depth range over the past two decades.

440
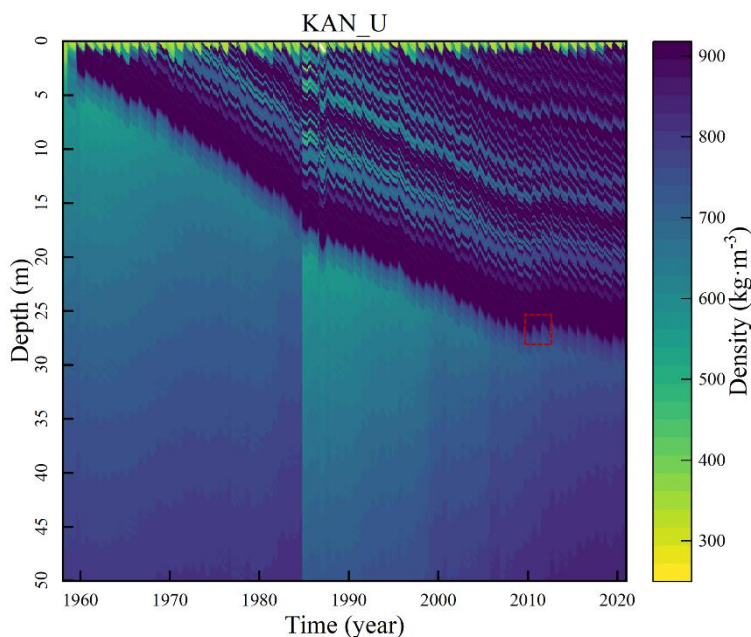
Figure 5. Time series of modelled firn depth-density profiles at KAN_U (1958-2020).

Taking liquid water percolation and phase transition into account, the model captures the high-density peaks ($\sim$917 $\mathrm{kg \cdot m^{-3}}$)
445   caused by the refreezing of liquid water. Within the 1-10 m depth range, the modelled firn density experiences a relatively

slight variability, fluctuating primarily between 760 $\mathrm{kg \cdot m^{-3}}$ and 917 $\mathrm{kg \cdot m^{-3}}$ (Fig. 6). The average modelled firn density

is 797.77 $\mathrm{kg \cdot m^{-3}}$ for the 1-5 m layer and 868.17 $\mathrm{kg \cdot m^{-3}}$ for the 6-10 m layer (Table 3). These high-density layers in the

top few meters of the column correspond to the formation of ice lenses or ice layers. Moreover, the variability of modelled firn

density increases in depths exceeding 10 m, showing fluctuations spanning from 700 $\mathrm{kg \cdot m^{-3}}$ to 917 $\mathrm{kg \cdot m^{-3}}$, with an

450   average density of 837.68 $\mathrm{kg \cdot m^{-3}}$. Beyond a depth of 10 m, there is an increase in variability in firn density and a decrease

in average density ($\sim$30.49 $\mathrm{kg \cdot m^{-3}}$) compared to the depth range of 6-10 m, which possibly is attributed to the limited liquid

water at depth. On the one hand, the firn densification model does not prevent the liquid water from percolating through ice

layers within 0.5 m depth, and thereby, liquid water refreezing continues to occur at depth and to densify the firn there. On the

other hand, the permeability of the firn layer decreases after the formation of ice lenses or ice layers, resulting in less liquid

455   water at depth compared to the liquid water at the upper layers of the firn column.
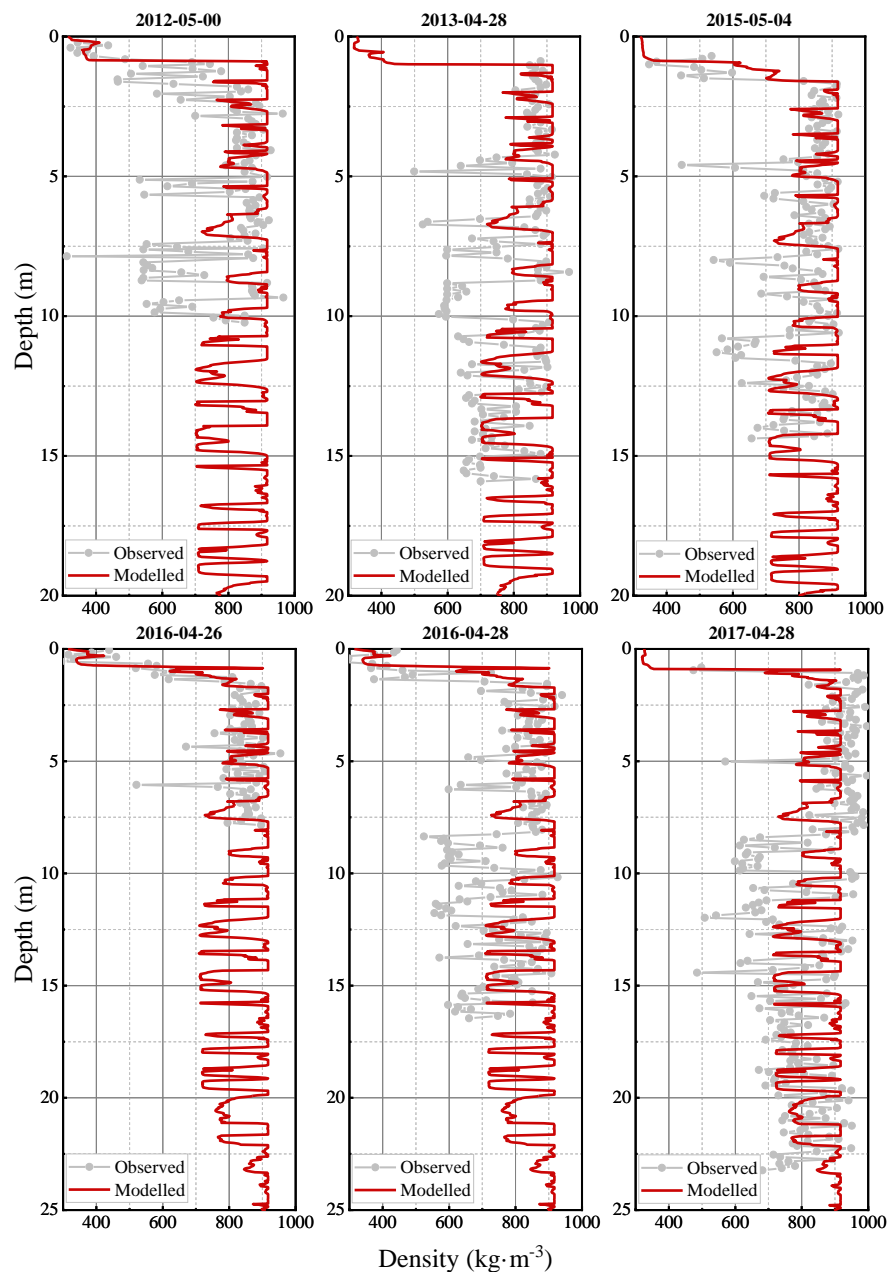
Figure 6. Observed (gray dotted line) and modelled (red solid line) firn depth-density profiles at KAN_U.

460   In comparison with observations from firn cores, the modelled density profiles reproduce the occurrence of ice slabs and compare well within uncertainties to punctual in situ measurements independent of the depth range. In accordance with Fig. 6, the observed firn density profiles varied in depth from 7.8 m to 23.19 m, and each of them revealed a thick, almost continuous ice slab in the upper parts of the firn column. Below the ice slab, numerous high-density layers separated by considerably

lower-density layers are apparent in the observations. In the depth range of 1-5 m, the simulations and observations exhibit an
465   exceptionally close agreement, with a deviation of 3.14 $\mathrm{kg \cdot m^{-3}}$ (Table 3). Even though variability in firn density is slightly
underestimated below the observed ice slab, the model agrees relatively well with observations within uncertainties. The
deviation between the average observed firn density and the average modelled firn density is 77.64 $\mathrm{kg \cdot m^{-3}}$ for the 6-10 m
range and 71.69 $\mathrm{kg \cdot m^{-3}}$ for the range beyond 10 m.

470   **Table 3. The average observed and modelled firn density over the 1-5, 6-10 and beyond 10 m depth ranges at KAN_U, as well as
their deviation.**

Depth range (m)	The average observed firn density ($\mathrm{kg \cdot m^{-3}}$)	The average modelled firn density ($\mathrm{kg \cdot m^{-3}}$)	Deviation ($\mathrm{kg \cdot m^{-3}}$)
1-5	794.63	797.77	3.14
6-10	790.53	868.17	77.64
10-End	765.99	837.68	71.69

4.1.2 Dye-2

As mentioned in Sect. 2.2, Dye-2 experiences a lower amount of snowmelt than KAN_U (145.79 mm w.e. yr^{-1}). The high-
475   density layers caused by water refreezing are, therefore, fewer at this location, leading to more variability between layers (Fig.
7). At Dye-2, a thickening of approximately 32.69 m from 1958 to 2020 is simulated, which is greater than that of KAN_U.
This difference is possibly attributed to Dye-2 having slightly lower temperatures and snowfall rates than KAN_U, while its
snowmelt rates are close to half that of KAN_U. From 2006 onwards, some ice lenses or ice layers began to form densely in
the top few meters of the firn column due to increased liquid water. Subsequently, these ice lenses or ice layers were advected
480   downward. The trend in firn density evolution remained relatively stable before 2010. Between 2010 and 2012, a pronounced
thinning (~ 0.25 m) was observed, after which the trend in density evolution returned to stability. In 2019, a minor thinning
event occurred. These thinning events were associated with increased surface temperature in 2010, 2012, and 2019, as well as
an increase in snowmelt and a slight reduction in snowfall.
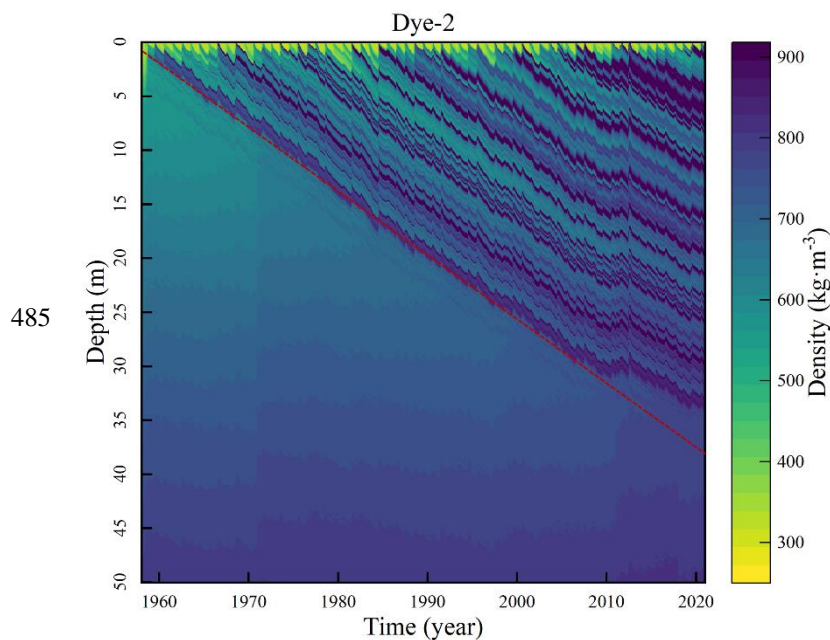
Figure 7. Time series of modelled firn depth-density profiles at Dye-2 (1958-2020)

At the Dye-2 site, the modelled depth-density profiles are observed with temporal variability and large inter-layer variability (Fig. 8). Moreover, the modelled profiles exhibit the features of high-density layers resulting from refreezing, especially in the first few meters of the firn column. Specifically, the modelled firn density typically occurs within the range of 640 to 917 $kg \cdot m^{-3}$, undergoing a substantial span. In accordance with Table 4, the average modelled firn density is 716.05 $kg \cdot m^{-3}$ for the depth range of 1-5 m, 768.38 $kg \cdot m^{-3}$ for the 6-10 m depth range, and 784.33 $kg \cdot m^{-3}$ for depths beyond 10 m. Unlike at the KAN_U site, the average densities at Dye-2 increase with depth, indicating that the firn densification at Dye-2 is primarily driven by the growth and deformation of firn grains.

For the high-density layers caused by refreezing into ice, the modelled density profiles correspond relatively well to the observed density profiles at all depth ranges. As can be seen in Fig. 8, the simulations are approximately consistent with observations in the first meter of the firn column, where fresh-snow density plays a crucial role. Particularly for the firn core of 2018-05-09, the model reproduces the high-density layer observed at around 0.9 m depth in the core. Additionally, both the modelled and observed density profiles are superimposed with sequences of higher and lower density peaks. The simulation compares relatively well with high-density peaks. Regrettably, observed density profiles have low peak densities that are smaller than the modelled values, especially in the shallow 5 m depth. Thus, the model underestimates the inter-layer variability of observations, and the overall firn density is overestimated by the simulations at Dye-2.
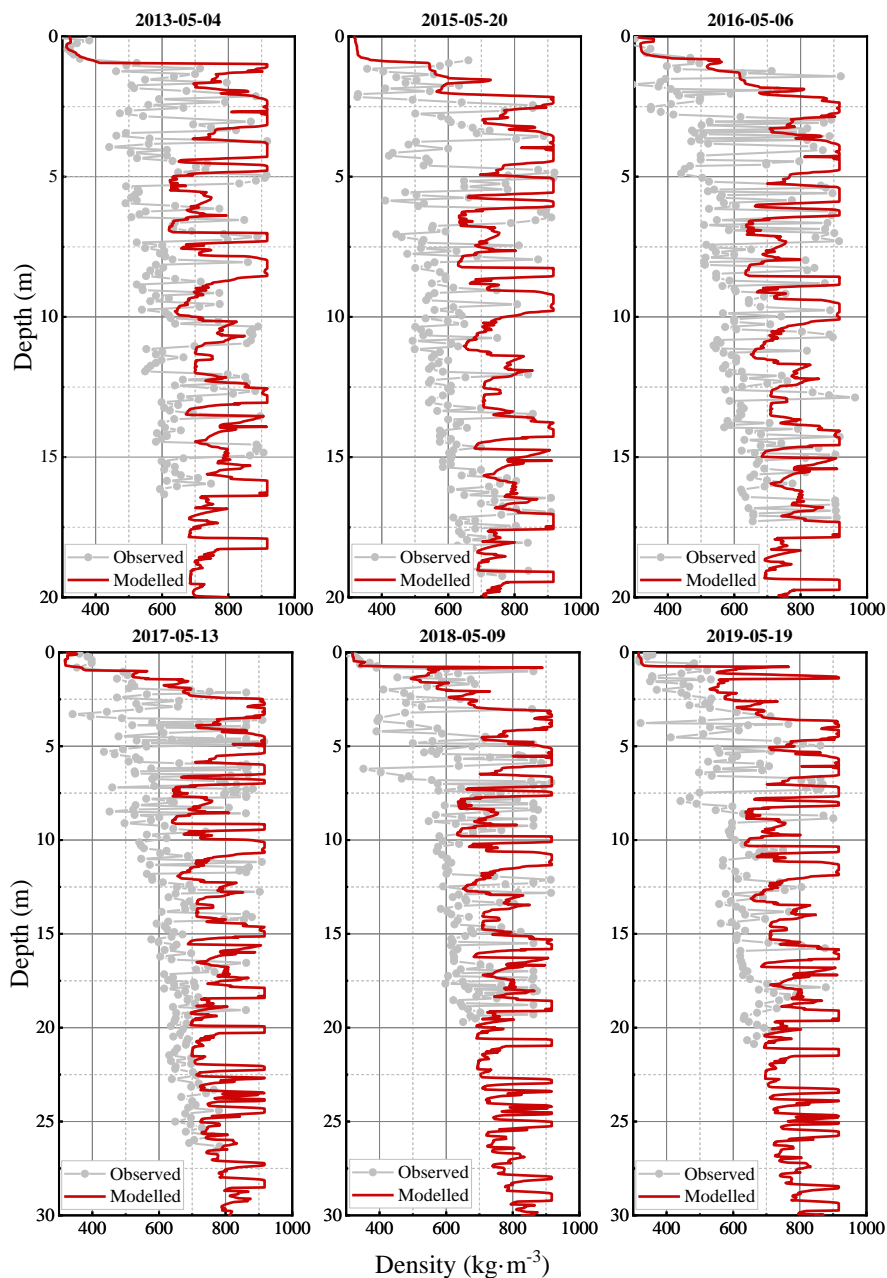
Figure 8. Observed (gray dotted line) and modelled (red solid line) firn depth-density profiles at Dye-2.

Table 4. The average observed and modelled firn density over the 1-5, 6-10 and beyond 10 m depth ranges at Dye-2, as well as their deviation.

Depth range (m)	The average observed	The average modelled	Deviation (kg · m^{-3})

	firn density (kg · m^{-3})	firn density (kg · m^{-3})	
1-5	576.54	716.05	139.51
6-10	666.94	768.38	101.44
10-End	681.86	784.33	102.47

510

4.2 Runoff and refreezing

We quantitatively assess the amount of runoff and refreezing in model outputs at KAN_U and Dye-2 (Fig. 9). As can be seen by combining Figs. 2, 3, and 9, the amount of liquid water entering the firn column at each time step directly influences the distribution proportion of liquid water among retention, refreezing, and runoff. At Dye-2, refreezing remains steady from 1958

515 to 2020, and minor or almost zero runoff occurred between 1958 and 2006. In the high liquid water years of 2007 and 2012, some liquid water was retained or refrozen, and the excess liquid water ran off, resulting in peak runoff observed in these two years. In the relatively high-melt KAN_U site, the refreezing remained relatively stable in most years apart from 2010 and 2012, in which the refreezing slightly decreased. The runoff also reached its maximum during the years 2010 to 2012, peaking at 830.62 mm w.e. yr^{-1} in 2012. These phenomena were likely attributed to the immediate formation of ice layers in the

520 uppermost layer of the firn column as a result of substantial liquid water refreezing in 2010 and 2012. Subsequently, these newly formed ice layers prevented the remaining liquid water from further percolating into the firn column, thereby promoting the runoff of liquid water.
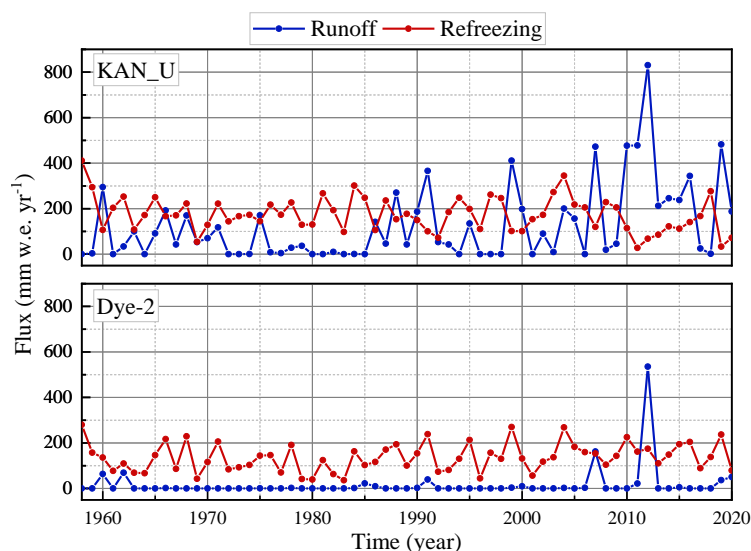
525 **Figure 9. Runoff and refreezing in model outputs at KAN_U and Dye-2 sites.**

5 Discussion

5.1 Relevant research analysis

In this section, we compare the results obtained at KAN_U and Dye-2 with previous firn modelling studies at these two sites. The model of Kuipers Munneke et al. (2015), abbreviated as the KM model, is a semi-empirical model designed for simulating

530 firn compaction, water percolation, and refreezing of the GrIS. For the dry-firn compaction, the KM model employs the expressions from Arthern et al. (2010). The downward percolation of liquid water is modelled by the Bucket scheme, which treats the irreducible water of each firn layer as the layer's liquid water. The results of the KM model do not capture the extensive density fluctuations resulting from the refreezing of liquid water, which could be attributed to the KM model's oversight of specific physical mechanisms related to liquid water infiltration. Our firn densification model utilizes Darcy's law

535 to simulate the infiltration of liquid water and, in conjunction with the Bucket scheme, assesses the liquid water content within each firn layer, making it more sensitive to the formation of ice lenses or ice layers.

Langen et al. (2017) utilized the CROCUS densification scheme (Vionnet et al., 2012) and a water flow program based on Darcy's law in their model. Commencing from a depth of 4 m, modelled firn density remains stable at roughly 800 $\mathrm{kg\ m^{-3}}$ at

540 KAN_U and 700 $\mathrm{kg\ m^{-3}}$ at Dye-2, which does not capture the observed extensive density fluctuations. A contributing factor to these inappropriate predictions of firn density may be the coarser resolution, assuming the layer thickness increases exponentially with depth and the initial depth is 0.065 m. These coarser resolutions may lead to the neglect of thin ice lenses or ice layers. We, therefore, adopt the initial layer thickness of 0.015 m w.e. for KAN_U and 0.014 m w.e. for Dye-2, which enables a better representation of thin ice lenses or ice layers. In addition, the remaining layer thickness exhibits slight

545 fluctuations around the initial layer thickness, correlated with the mass and density of the firn layer.

Verjans et al. (2019) implemented three water percolation schemes: the Bucket approach, the Richards equation in a single domain, and the Richards equation in a dual domain. The dual-domain Richards equation accounts for partitioning between matrix and preferential flow. Their results show that the Bucket scheme is as efficient in replicating observed density profiles

550 as the single-domain Richards equation, and the most physically detailed dual-domain scheme does not improve upon the Bucket scheme method when compared to observations. As such, considering preferential flow mechanisms may introduce additional errors to firn densification models until the physical processes in preferential flow are clearly understood. All of the flow schemes do not capture the high-density layers observed in measured depth-density profiles at KAN_U. Furthermore, all three flow schemes are found to underestimate the density fluctuations caused by ice lenses or ice layers and overestimate the

555 dominant trend of firn density evolution at Dye-2. Verjans et al. (2019) pointed out that the underestimation of firn density variability may stem from the fact that one or several factors that play a significant role in firn evolution are either rarely or not considered by the firn densification model. These factors may include variability in fresh-snow density, the effects of firn microstructure and impurity content on densification, wind packing and short-term weather fluctuations. Building upon this

perspective, we calculate the fresh-snow density using a parameterized empirical formula that inherently considers the

560   influence of climatic fluctuations and impurities on fresh-snow density. Additionally, we set the time step as the time required

to accumulate an equivalent amount of snowfall, reducing the impact of short-term weather fluctuations on firn densification.

Moreover, the validity of the firn densification mainly relies on the accuracy of the climatic forcing. Therefore, we apply the

1 km downscaled data from the RACMO2.3p2 model, which is widely evaluated and considered suitable as a forcing data set

on polar ice sheets.

565

Thompson-Munson et al. (2023) executed two firn models, the physics-based SNOWPACK model and the Community Firn

Model (CFM; Stevens et al., 2020) configured with a semi-empirical densification equation (CFM-GSFC), to predict firn

densities across the GrIS from 1980 to 2020. The Bucket scheme was used for both firn models to handle water percolation

and refreezing. In their study, both firn models successfully replicated the high-density layers resulting from the extreme

570   melting event of 2012 while not capturing the high-density layers in other years. Compared to CFM-GSFC, SNOWPACK

simulated more significant inter-layer variability. The disparity is partly attributed to the fact that the CFM-GSFC model uses

a fixed fresh-snow density of 350 kg m^{-3}, whereas the SNOWPACK model employs a fresh-snow density that varies with

atmospheric conditions, and partly to the CFM-GSFC outputs being interpolated onto a 0.25 m grid. Actually, the higher

vertical resolution of a few centimeters per layer is required in the near-surface layers, where the firn is more sensitive to short-

575   term atmospheric fluctuations. Hence, model outputs are interpolated onto a 0.01 m regular grid for the initial 20 m and a 0.025

m regular grid for the remaining depth in this study. Moreover, the significance of fresh-snow density is further illustrated in

the research of Thompson-Munson et al. (2023). Future research should further develop semi-empirical parameterization

equations based on various meteorological data and potential physical mechanisms to simulate fresh-snow density more

accurately.

580   **5.2 Model limitations and potential improvements**

Despite the overall good agreement between the observed and modelled density profiles predicted by our firn densification

model, limitations can also be identified. At the KAN_U site, a region characterized by pronounced liquid water, the firn

densification model exhibits high performance within uncertainties at all depth ranges, reproducing the occurrence of ice slabs

in line with observations, especially in the first few meters of the firn column (Fig. 6 and Table 3). Below the ice slab, the

585   deviation between observations and simulations exhibits a slight increase, presumably as a result of excess refreezing at depth.

Similarly, at Dye-2 with limited liquid water, the model captures the features of high-density layers while overestimating low-

density peaks, possibly attributed to excess refreezing of liquid water. The overall performance of the model at KAN_U

exceeds that at Dye-2, which may be associated with more substantial liquid water at KAN_U. As described in Sect. 4.2, the

amount of liquid water entering the firn column at each time step directly influences the distribution proportion of liquid water

590   among retention, refreezing, and runoff. In areas with limited liquid water, it is more challenging to simulate the liquid water

content within each firn layer accurately, and thus, excess refreezing is more likely to occur.

The following two factors are probably responsible for the excess refreezing: (i) the Lagrangian stratification approach and (ii) the overlook of heterogeneous percolation. In this study, liquid water is assumed to percolate along the firn column layer by layer, potentially partitioning a pore space across multiple firn layers. This percolation scheme enables liquid water to exist in each firn layer before the maximum percolation depth is attained, thus probably overestimating the refreezing volume and resulting in an inappropriate estimation of the refreezing depth.

Heterogeneous percolation induced by ice crevasses is not considered in our simulation. A significant contributor to the neglect of heterogeneous percolation is the limited understanding of preferential flow, which, if included, might potentially bring further uncertainty (Verjans et al., 2019). Since preferential flow has the ability to transfer water below ice layers, it is possible that liquid water is absent from a firn layer but rather exists in the layer beneath. This phenomenon may result in low densities in some firn layers, while the layer below them undergoes a rise in density as a result of ice lenses or ice layers, as observed in measured depth-density profiles. Therefore, it is of utmost importance to enhance the exploration of preferential flow measurements and numerical simulations in future studies, and subsequently, employ them in firn densification modelling.

Furthermore, the limited knowledge of how the ice lens or ice layer persists in the deep firn layer after formation may also lead to the overestimation of low-density peaks. In this research, after ice lenses or ice layers are formed, we just displace the firn layer in a downward direction in the next time step without employing any additional mechanisms. However, power-law creep mechanisms or shear forces may induce the newly formed thin ice lenses or ice layers to break, consequently leading to a decrease in the density of the underlying firn layers compared to the direct movement. Furthermore, we acknowledge that the calculation of firn grain sizes in Sect. 3.3 involves various idealized assumptions, and firn grains cannot be precisely simulated using only those simplified equations. Unfortunately, the development of firn microstructure is not sufficiently understood at present. In future firn densification modelling, machine learning methods should be considered to reduce the uncertainties introduced by poorly understood firn densification processes.

6 Conclusion

In this study, an improved firn densification model has been developed from the perspective of elucidating liquid water percolation and phase-change mechanisms. This model accounts for fresh-snow density variability, initial grain size variability, grain size growth, density-dependent and temperature-dependent thermal conductivity, dry-firn compaction, state-dependent hydraulic conductivity, retention, refreezing, and runoff. The capillary retention, refreezing, and runoff of liquid water are assessed by integrating the Bucket scheme and Darcy's law. Variable physical quantities are more in line with the actual physical characteristics of firn than constant ones. For example, setting fresh-snow density according to the parameterization of Fausto et al. (2018), rather than a constant value like 350 kg m^{-3}, allows for variability in fresh-snow density at different

sites or within the same site. In addition, the time step is set as the time required to accumulate an equal amount of snowfall
625 rather than a constant value, reducing the impact of short-term weather fluctuations on firn densification. Moreover, the improved model was employed for two study sites, KAN_U and Dye-2, over the GrIS to evaluate its performance.

Diverging from previous firn densification models, comparison with 12 firn cores shows that using the Coléou and Lesaffre (1998) parameterization in combination with Darcy's flow law allows for the formation of ice lenses or ice layers in agreement
630 with observations, which reproduces high-density peaks at these two sites. In general, the model compares relatively well with observations. Especially at the KAN_U site, the simulations and observations exhibit a close agreement within the range of uncertainties, with a deviation of 3.14 $\mathrm{kg \cdot m^{-3}}$ for the 1-5 m range, 77.64 $\mathrm{kg \cdot m^{-3}}$ for the 6-10 m range, and 71.69 $\mathrm{kg \cdot m^{-3}}$ for the range beyond 10 m. Nevertheless, imperfections are still present in the firn densification model, particularly at Dye-2, where liquid water is limited. Specifically, the observed low-density peaks are overestimated, and the inter-layer
635 variability in firn density is underestimated, possibly as a result of excess refreezing.

In areas with limited liquid water, it is more challenging to accurately simulate the percolation and refreezing within each firn layer, and thus, excess refreezing is more likely to occur. The following two factors are probably responsible for the excess refreezing: (i) the Lagrangian stratification approach and (ii) the overlook of heterogeneous percolation. Therefore, it is
640 necessary to enhance the measurements and further improve numerical simulations of heterogeneous percolation in future studies, and subsequently, employ them in firn densification modelling. Furthermore, the overestimation of low-density peaks may also be caused by the limited knowledge of how the ice lens or ice layer persists in the deep firn layer after formation. In future firn densification modelling, machine learning methods should be considered to integrate data-driven and physical mechanisms, reducing uncertainties arising from poorly understood firn densification processes.

645

Code and Data availability. The RACMO2.3p2 data is available from B. Noël without conditions (Noël et al., 2018). The SUMup dataset can be found at https://doi.org/10.18739/A2NP1WK6M (Thompson-Munson et al., 2022). The Community Firn Model code is publicly available under the MIT license at https://doi.org/10.5281/zenodo.8083362 (Stevens et al., 2023).

650 *Author contribution*. Xueyu Zhang completed the modelling work and wrote the original manuscript. Lin Liu designed the research together with Zhicai Luo and supervised the work. Brice Noël processed and provided the RACMO2.3p2 forcing data. All the authors contributed to the analysis, interpretation of the results and provided feedback on the final manuscript.

Competing interests. The authors declare that they have no conflict of interest.

655

Acknowledgements. This research was financially supported by the National Natural Science Foundation of China (grant nos. 42274028 and 41704023). B. Noël was funded by the Fonds de la Recherche Scientifique de Belgique (F.R.S.-FNRS). We

acknowledge Christopher Max Stevens for the open-source CFM framework and his assistance in modelling the firn densification model. We would also like to thank Megan Thompson-Munson for compiling the available SUMup dataset.

660

Refrences

Alley, R. B.: Firn densification by grain-boundary sliding: a first model, Journal de Physique Colloques, 48, C1-249-C1-256, https://doi.org/10.1051/jphyscol:1987135, 1987.

Arnaud, L., Barnola, J. M., and Duval, P.: Physical modeling of the densification of snow/firn and ice in the upper part of polar
665   ice sheets, Physics of ice core records, Hokkaido University Press, 285-305, http://hdl.handle.net/2115/32472, 2000.

Arthern, R. J., Vaughan, D. G., Rankin, A. M., Mulvaney, R., and Thomas, E. R.: In situ measurements of Antarctic snow compaction compared with predictions of models, J. Geophys. Res.-Earth, 115, F03011, https://doi.org/10.1029/2009JF001306, 2010.

Brils, M., Kuipers Munneke, P., van de Berg, W. J., and van den Broeke, M.: Improved representation of the contemporary
670   Greenland ice sheet firn layer by IMAU-FDM v1.2G, Geosci. Model Dev., 15, 7121-7138, https://doi.org/10.5194/gmd-15-7121-2022, 2022.

Buizert, C. and Severinghaus, J. P.: Dispersion in deep polar firn driven by synoptic-scale surface pressure variability, The Cryosphere, 10, 2099-2111, https://doi.org/10.5194/tc-10-2099-2016, 2016.

Calonne, N., Flin, F., Morin, S., Lesaffre, B., du Roscoat, S. R., and Geindreau, C.: Numerical and experimental investigations
675   of the effective thermal conductivity of snow, Geophys. Res. Lett., 38, L23501, https://doi.org/10.1029/2011GL049234, 2011.

Calonne, N., Geindreau, C., Flin, F., Morin, S., Lesaffre, B., Rolland du Roscoat, S., and Charrier, P.: 3-D image-based numerical computations of snow permeability: links to specific surface area, density, and microstructural anisotropy, The Cryosphere, 6, 939-951, https://doi.org/10.5194/tc-6-939-2012, 2012.

680 Calonne, N., Milliancourt, L., Burr, A., Philip, A., Martin, C. L., Flin, F., and Geindreau, C.: Thermal conductivity of snow, firn, and porous ice from 3-D image-based computations, Geophys. Res. Lett., 46, 13079-13089, https://doi.org/10.1029/2019GL085228, 2019.

Colbeck, S. C.: The capillary effects on water percolation in homogeneous snow, J. Glaciol., 13, 85-97, https://doi.org/10.3189/S002214300002339X, 1974.

685 Colbeck, S. C.: A theory for water flow through a layered snowpack, Water Resour. Res., 11, 261-266, https://doi.org/10.1029/WR011i002p00261, 1975.

Coléou, C. and Lesaffre, B.: Irreducible water saturation in snow: experimental results in a cold laboratory, Ann. Glaciol., 26, 6468, 1998.

Cuffey, K. M. and Paterson, W. S. B.: The Physics of Glaciers, 4th ed., Pergamon, Oxford, U. K, 40 pp., ISBN 978-0-12-
690   369461-4, 2010.

Fausto, R. S., Box, J. E., Vandecrux, B., van As, D., Steffen, K., MacFerrin, M. J., Machguth, H., Colgan, W., Koenig, L. S.,
McGrath, D., Charalampidis, C., and Braithwaite, R. J.: A Snow Density Dataset for Improving Surface Boundary
Conditions in Greenland Ice Sheet Firn Modeling, Front. Earth Sci., 6, 40-49, https://doi.org/10.3389/feart.2018.00051,
2018.

695   Fettweis, X., Hofer, S., Krebs-Kanzow, U., Amory, C., Aoki, T., Berends, C. J., Born, A., Box, J. E., Delhasse, A., Fujita, K.,
Gierz, P., Goelzer, H., Hanna, E., Hashimoto, A., Huybrechts, P., Kapsch, M.-L., King, M. D., Kittel, C., Lang, C., Langen,
P. L., Lenaerts, J. T. M., Liston, G. E., Lohmann, G., Mernild, S. H., Mikolajewicz, U., Modali, K., Mottram, R. H., Niwano,
M., Noël, B., Ryan, J. C., Smith, A., Streffing, J., Tedesco, M., van de Berg, W. J., van den Broeke, M., van de Wal, R. S.
W., van Kampenhout, L., Wilton, D., Wouters, B., Ziemen, F., and Zolles, T.: GrSMBMIP: intercomparison of the modelled
700   1980-2012 surface mass balance over the Greenland Ice Sheet, The Cryosphere, 14, 3935-3958, https://doi.org/10.5194/tc-
14-3935-2020, 2020.

Forster, R. R., Box, J. E., van den Broeke, M. R., Miège, C., Burgess, E. W., van Angelen, J. H., Lenaerts, J. T. M., Koenig,
L. S., Paden, J., Lewis, C., Gogineni, S. P., Leuschen, C., and McConnell, J. R.: Extensive liquid meltwater storage in firn
within the Greenland ice sheet, Nat. Geosci., 7, 95-98, https://doi.org/10.1038/ngeo2043, 2014.

705   Gow, A. J.: On the Rates of Growth of Grains and Crystals in South Polar Firn, J. Glaciol., 8, 241-252,
https://doi.org/10.3189/S0022143000031233, 1969.

Helm, V., Humbert, A., and Miller, H.: Elevation and elevation change of Greenland and Antarctica derived from CryoSat2,
The Cryosphere, 8, 1539-1559, https://doi.org/10.5194/tc-81539-2014, 2014.

Helsen, M. M., Van den Broeke, M. R., Van De Wal, R. S., Van De Berg, W. J., Van Meijgaard, E., Davis, C. H., Li, Y., and
710   Goodwin, I.: Elevation changes in antarctica mainly determined by accumulation variability, Science, 320, 1626-1629,
https://doi.org/10.1126/science.1153894, 2008.

Herron, M. M. and Langway, C. C.: Firn densification: an empirical model., J. Glaciol., 25, 373-385,
https://doi.org/10.1017/S0022143000015239, 1980.

Hirashima, H., Yamaguchi, S., Sato, A., and Lehning, M.: Numerical modeling of liquid water movement through layered
715   snow based on new measurements of the water retention curve, Cold Reg. Sci. Technol., 64, 94-103,
https://doi.org/10.1016/j.coldregions.2010.09.003, 2010.

Humphrey, N. F., Harper, J. T., and Pfeffer, W. T.: Thermal tracking of meltwater retention in Greenland's accumulation area,
J. Geophys. Res.-Earth Surf., 117, 1-11, https://doi.org/10.1029/2011JF002083, 2012.

Huss, M.: Density assumptions for converting geodetic glacier volume change to mass change, The Cryosphere, 7, 877-887,
720   https://doi.org/10.5194/tc-7-877-2013, 2013.

Jin, J., Gao, X., Yang, Z.-L., Bales, R. C., Sorooshian, S., Dickinson, R. E., Sun, S. F., and Wu, G. X.: Comparative Analyses of Physically Based Snowmelt Models for Climate Simulations, J. Climate, 12, 2643-2657, https://doi.org/10.1175/1520-0442(1999)012<2643:CAOPBS>2.0.CO;2, 1999.

Katsushima, T., Kumakura, T., and Takeuchi, Y.: A multiple snow layer model including a parameterization of vertical water channel process in snowpack, Cold Reg. Sci. Technol., 59, 143-151, https://doi.org/10.1016/j.coldregions.2009.09.002, 2009.

Keenan, E., Wever, N., Dattler, M., Lenaerts, J. T. M., Medley, B., Kuipers Munneke, P., and Reijmer, C.: Physics-based SNOWPACK model improves representation of near-surface Antarctic snow and firn density, The Cryosphere, 15, 1065-1085, https://doi.org/10.5194/tc-15-1065-2021, 2021.

Kuipers Munneke, P., Ligtenberg, S. R. M., Noël, B. P. Y., Howat, I. M., Box, J. E., Mosley-Thompson, E., McConnell, J. R., Steffen, K., Harper, J. T., Das, S. B., and van den Broeke, M. R.: Elevation change of the Greenland ice sheet due to surface mass balance and firn processes, 1960-2013, The Cryosphere, 9, 3541-3580, https://doi.org/10.5194/tcd-9-3541-2015, 2015.

Langen, P. L., Fausto, R. S., Vandecrux, B., Mottram, R. H., and Box, J. E.: Liquid Water Flow and Retention on the Greenland Ice Sheet in the Regional Climate Model HIRHAM5: Local and Large-Scale Impacts, Front. Earth Sci., 4, 110, https://doi.org/10.3389/feart.2016.00110, 2017.

Li, J. and Zwally, H. J.: Modeling the density variation in the shallow firn layer, Ann. Glaciol., 38, 309-313, https://doi.org/10.3189/172756404781814988, 2004.

Li, J. and Zwally, H. J.: Modeling of firn compaction for estimating ice-sheet mass change from observed ice-sheet elevation change, Ann. Glaciol., 52, 1–7, https://doi.org/10.3189/172756411799096321, 2011.

Ligtenberg, S. R. M., Helsen, M. M., and van den Broeke, M. R.: An improved semi-empirical model for the densification of Antarctic firn, The Cryosphere, 5, 809-819, https://doi.org/10.5194/tc-5809-2011, 2011.

Ligtenberg, S. R. M., Kuipers Munneke, P., Noël, B. P. Y., and van den Broeke, M. R.: Brief communication: Improved simulation of the present-day Greenland firn layer (1960–2016), The Cryosphere, 12, 1643–1649, https://doi.org/10.5194/tc-12-1643-2018, 2018.

Linow, S., Hörhold, M., and Freitag, J.: Grain-size evolution of polar firn: A new empirical grain growth parameterization based on X-ray microcomputer tomography measurements, J. Glaciol., 58, 1245-1252, https://doi.org/10.3189/2012JoG11J256, 2012.

Lu, F., You, W., Fan, D.-M.: Analysis of Greenland Ice mass change based on GRACE, J. Geod. Geodyn., 35, 640-644, https://doi.org/10.14075/j.jgg.2015.04.021, 2015.

Lundin, J. M., Stevens, C. M., Arthern, R., Buizert, C., Orsi, A., Ligtenberg, S. R., Simonsen, S. B., Cummings, E., Essery, R., Leahy, W., Harris, P., Helsen, M. M., and Waddington, E. D.: Firn Model Intercomparison Experiment (FirnMICE), J. Glaciol., 63, 401-422, https://doi.org/10.1017/jog.2016.114, 2017.

MacFerrin, M., Machguth, H., van As, D., Charalampidis, C., Stevens, C. M., Heilig, A., Vandecrux, B., Langen, P. L., Mottram, R., Fettweis, X., Van den Broeke, M. R., Pfeffer, W. T., Moussavi, M., and Abdalati, W.: Rapid expansion of Greenland's low-permeability ice slabs, Nature, 573, 403-407, https://doi.org/10.1038/s41586-019-1550-3, 2019.

MacFerrin, M. J., Stevens, C. M., Vandecrux, B., Waddington, E. D., and Abdalati, W.: The Greenland Firn Compaction Verification and Reconnaissance (FirnCover) dataset, 2013-2019, Earth Syst. Sci. Data, 14, 955-971, https://doi.org/10.5194/essd-14955-2022, 2022.

Machguth, H., MacFerrin, M., van As, D., Box, J. E., Charalampidis, C., Colgan, W., Fausto, R. S., Meijer, H. A. J., Mosley-Thompson, E., and van de Wal, R. S. W.: Greenland meltwater storage in firn limited by near-surface ice formation, Nat. Clim. Change, 6, 390-393, https://doi.org/10.1038/nclimate2899, 2016.

Morris, E. M. and Wingham, D. J.: Uncertainty in massbalance trends derived from altimetry: a case study along the EGIG line, central Greenland, J. Glaciol., 61, 345-356, https://doi.org/10.3189/2015JoG14J123, 2015.

Mualem, Y.: A new model for predicting the hydraulic conductivity of unsaturated porous media, Water Resour. Res., 12, 513-522, https://doi.org/10.1029/WR012i003p00513, 1976.

Nghiem, S. V., Hall, D. K., Mote, T. L., Tedesco, M., Albert, M. R., Keegan, K., Shuman, C. A., DiGirolamo, N. E., and Neumann, G.: The extreme melt across the Greenland ice sheet in 2012, Geophys. Res. Lett., 39, 6-11, https://doi.org/10.1029/2012GL053611, 2012.

Noël, B., van de Berg, W. J., van Wessem, J. M., van Meijgaard, E., van As, D., Lenaerts, J. T. M., Lhermitte, S., Kuipers Munneke, P., Smeets, C. J. P. P., van Ulft, L. H., van de Wal, R. S. W., and van den Broeke, M. R.: Modelling the climate and surface mass balance of polar ice sheets using RACMO2 - Part 1: Greenland (1958-2016), The Cryosphere, 12, 811-831, https://doi.org/10.5194/tc-12-811-2018, 2018.

Noël, B., van de Berg, W. J., Lhermitte, S., and van den Broeke, M. R.: Rapid ablation zone expansion amplifies north Greenland mass loss, Sci. Adv., 5, 2-11, https://doi.org/10.1126/sciadv.aaw0123, 2019.

Pfeffer, W. T. and Humphrey, N. F.: Determination of timing and location of water movement and ice-layer formation by temperature measurements in sub-freezing snow, J. Glaciol., 42, 292-304, https://doi.org/10.3189/S0022143000004159, 1996.

Reid, R. C., Sherwood, T. K., and Street, R. E.: The Properties of Gases and Liquids, Phys. Today, 12, 38-40, https://doi.org/10.1063/1.3060771, 1959.

Reijmer, C. H., van den Broeke, M. R., Fettweis, X., Ettema, J., and Stap, L. B.: Refreezing on the Greenland ice sheet: a comparison of parameterizations, The Cryosphere, 6, 743-62, https://doi.org/10.5194/tc-6-743-2012, 2012.

Richards, L.: Capillary conduction of liquids through porous mediums, J. Appl. Phys., 1, 318-333, https://doi.org/10.1063/1.1745010, 1931.

Schwerdtfeger, P.: Theoretical derivation of the thermal conductivity and diffusivity of snow, General Assembly of Berkeley Commission of Snow and Ice, 61, 75-81, 1963.

Shepherd, A., Ivins, E. R., Geruo, A., Barletta, V. R., Bentley, M. J., Bettadpur, S., Briggs, K. H., Bromwich, D. H., Forsberg, R., and Galin, N.: A reconciled estimate of ice-sheet mass balance, Science, 338, 1183-1189, https://doi.org/10.1126/science.1228102, 2012.

Shepherd, A., Ivins, E., Rignot, E., Smith, B., van den Broeke, M., Velicogna, I., Whitehouse, P., Briggs, K., Joughin, I.,
790   Krinner, G., Nowicki, S., Payne, T., Scambos, T., Schlegel, N., A, G., Agosta, C., Ahlstrøm, A., Babonis, G., Barletta, V. R., Bjørk, A. A., Blazquez, A., Bonin, J., Colgan, W., Csatho, B., Cullather, R., Engdahl, M. E., Felikson, D., Fettweis, X., Forsberg, R., Hogg, A. E., Gallee, H., Gardner, A., Gilbert, L., Gourmelen, N., Groh, A., Gunter, B., Hanna, E., Harig, C., Helm, V., Horvath, A., Horwath, M., Khan, S., Kjeldsen, K. K., Konrad, H., Langen, P. L., Lecavalier, B., Loomis, B., Luthcke, S., McMillan, M., Melini, D., Mernild, S., Mohajerani, Y., Moore, P., Mottram, R., Mouginot, J., Moyano, G.,
795   Muir, A., Nagler, T., Nield, G., Nilsson, J., Noël, B., Otosaka, I., Pattle, M. E., Peltier, W. R., Pie, N., Rietbroek, R., Rott, H., Sandberg Sørensen, L., Sasgen, I., Save, H., Scheuchl, B., Schrama, E., Schröder, L., Seo, K. W., Simonsen, S. B., Slater, T., Spada, G., Sutterley, T., Talpe, M., Tarasov, L., van de Berg, W. J., van der Wal, W., van Wessem, M., Vishwakarma, B. D., Wiese, D., Wilton, D., Wagner, T., Wouters, B., and Wuite, J.: Mass balance of the Greenland Ice Sheet from 1992 to 2018, Nature, 579, 233-239, https://doi.org/10.1038/s41586-019-1855-2, 2020.

800   Shimizu, H.: Air permeability of deposited snow. Contribut. Instit. Low Temp. Sci., A22, 1-32, http://hdl.handle.net/2115/20234, 1970.

Simonsen, S. B., Stenseng, L., Adalgeirsdottir, G., Fausto, R. S., Hvidberg, C. S., and Lucas-Picher, P.: Assessing a multilayered dynamic firn-compaction model for Greenland with ASIRAS radar measurements, J. Glaciol., 59, 545–558, https://doi.org/10.3189/2013JoG12J158, 2013.

805   Smith, B., Fricker, H. A., Gardner, A. S., Medley, B., Nilsson, J., Paolo, F. S., Holschuh, N., Adusumilli, S., Brunt, K., and Csatho, B.: Pervasive ice sheet mass loss reflects competing ocean and atmosphere processes, Science, 368, 1239-1242, https://doi.org/10.1126/science.aaz5845, 2020.

Steger, C. R., Reijmer, C. H., and van den Broeke, M. R.: The modelled liquid water balance of the Greenland Ice Sheet, The Cryosphere, 11, 2507–2526, https://doi.org/10.5194/tc-11-25072017, 2017.

810   Stevens, C. M.: Investigations of physical processes in polar firn through modeling and field measurements, Ph.D. thesis, University of Washington, Seattle, 159 pp., 2018.

Stevens, C. M., Verjans, V., Lundin, J. M. D., Kahle, E. C., Horlings, A. N., Horlings, B. I., and Waddington, E. D.: The Community Firn Model (CFM) v1.0, Geosci. Model Dev., 13, 4355-4377, https://doi.org/10.5194/gmd-13-4355-2020, 2020.

Stevens, C. M., Lilien, D. A., Conway, H., Fudge, T. J., Koutnik, M. R., and Waddington, E. D.: A new model of dry
815   firndensification constrained by continuous strain measurements near South Pole, J. Glaciol., 1-15, https://doi.org/10.1017/jog.2023.87, 2023.

Stevens, C. M., Vo, H., emmakahle, Jboat, and oraschewski: UWGlaciology/CommunityFirnModel: Version 2.2.0, Zenodo [code], https://doi.org/10.5281/zenodo.8083362, 2023.

Sturm, M., Holmgren, J., König, M., and Morris, K.: The thermal conductivity of seasonal snow, J. Glaciol., 43, 26-41,
820   https://doi.org/10.3189/S0022143000002781, 1997.

Tedesco, M. and Fettweis, X.: Unprecedented atmospheric conditions (1948–2019) drive the 2019 exceptional melting season
      over the Greenland ice sheet, The Cryosphere, 14, 1209–1223, https://doi.org/10.5194/tc-14-1209-2020, 2020.

Thompson-Munson, M., Montgomery, L., Lenaerts, J., and Koenig, L.: Surface Mass Balance and Snow Depth on Sea Ice
      Working Group (SUMup) snow density subdataset, Greenland and Antartica, 1952–2019, Arctic Data Center [data set],
825   https://doi.org/10.18739/A2NP1WK6M, 2022.

Thompson-Munson, M., Wever, N., Stevens, C. M., Lenaerts, J. T. M., and Medley, B.: An evaluation of a physics-based firn
      model and a semi-empirical firn model across the Greenland Ice Sheet (1980-2020), The Cryosphere, 17, 2185-2209,
      https://doi.org/10.5194/tc-17-2185-2023, 2023.

Vandecrux, B., Fausto, R. S., van As, D., Colgan, W., Langen, P. L., Haubner, K., Ingeman-Nielsen, T., Heilig, A., Stevens,
830   C. M., MacFerrin, M., Niwano, M., Steffen, K., and Box, J.: Firn cold content evolution at nine sites on the Greenland
      ice sheet between 1998 and 2017, J. Glaciol., 66, 1-12, https://doi.org/10.1017/jog.2020.30, 2020a.

Vandecrux, B., Mottram, R., Langen, P. L., Fausto, R. S., Olesen, M., Stevens, C. M., Verjans, V., Leeson, A., Ligtenberg, S.,
      Kuipers Munneke, P., Marchenko, S., van Pelt, W., Meyer, C. R., Simonsen, S. B., Heilig, A., Samimi, S., Marshall, S.,
      Machguth, H., MacFerrin, M., Niwano, M., Miller, O., Voss, C. I., and Box, J. E.: The firn meltwater Retention Model
835   Intercomparison Project (RetMIP): evaluation of nine firn models at four weather station sites on the Greenland ice sheet,
      The Cryosphere, 14, 3785-3810, https://doi.org/10.5194/tc-14-3785-2020, 2020b.

van Dalum, C. T., van de Berg, W. J., and van den Broeke, M. R.: Impact of updated radiative transfer scheme in snow and
      ice in RACMO2.3p3 on the surface mass and energy budget of the Greenland ice sheet, The Cryosphere, 15, 1823-1844,
      https://doi.org/10.5194/tc-15-1823-2021, 2021.

840 van Dusen, M. S., and Washburn, E. W.: Thermal conductivity of non-metallic solids, International critical tables of numerical
      data, physics, chemistry and technology, New York: McGraw-Hill, 216-217, 1929.

van Genuchten, M.: A closed form equation for predicting the hydraulic conductivity of unsaturated soils., Soil Sci. Soc. Am.
      J., 44, 892-898, https://doi.org/10.2136/sssaj1980.03615995004400050002x, 1980.

Verjans, V., Leeson, A. A., Stevens, C. M., MacFerrin, M., Noël, B., and van den Broeke, M. R.: Development of physically
845   based liquid water schemes for Greenland firn-densification models, The Cryosphere, 13, 1819-1842,
      https://doi.org/10.5194/tc-13-1819-2019, 2019.

Vionnet, V., Brun, E., Morin, S., Boone, A., Faroux, S., Le Moigne, P., Martin, E., and Willemet, J. M.: The detailed snowpack
      scheme CROCUS and its implementation in SURFEX v7.2, Geosci. Model Dev., 5, 773-791,
      https://doi.org/10.5194/gmd-5773-2012, 2012.

850 Wever, N., Würzer, S., Fierz, C., and Lehning, M.: Simulating ice layer formation under the presence of preferential flow in
      layered snowpacks, The Cryosphere, 10, 2731-2744, https://doi.org/10.5194/tc-10-2731-2016, 2016.

Yamaguchi, S., Katsushima, T., Sato, A., and Kumakura, T.: Water retention curve of snow with different grain sizes. Cold Reg. Sci. Technol., 64, 87-93. https://doi.org/10.1016/j.coldregions.2010.05.008, 2010.

Yen, Y.-C.: Review of the thermal properties of snow, ice and sea ice, Tech. Rep. 81-10, Cold Regions Research and
855   Engineering Laboratory, Hanover, NH, USA, 27 pp. 1981.

Zwally, H. J. and Li, J.: Seasonal and interannual variations of firn densification and ice-sheet surface elevation at the Greenland summit, J. Glaciol., 48, 199-207, https://doi.org/10.3189/172756502781831403, 2002.